Standing surface acoustic waves in $LiNbO_3$ studied by time resolved X-ray diffraction at Petra III

T. Reusch, F. Schülein, C. Bömer, M. Osterhoff, A. Beerlink, H. J. Krenner, A. Wixforth, and T. Salditt

Citation: AIP Advances **3**, 072127 (2013); doi: 10.1063/1.4816801
View online: https://doi.org/10.1063/1.4816801
View Table of Contents: http://aip.scitation.org/toc/adv/3/7
Published by the American Institute of Physics

Standing surface acoustic waves in $LiNbO_3$ studied by time resolved X-ray diffraction at Petra III

T. Reusch,[1,a] F. Schülein,[2] C. Bömer,[1] M. Osterhoff,[1] A. Beerlink,[3]
H. J. Krenner,[2] A. Wixforth,[2] and T. Salditt[1,b]
[1]*Institut für Röntgenphysik, Georg-August Universität Göttingen, Friedrich Hund Platz 1, Göttingen, Germany*
[2]*Lehrstuhl für Experimentalphysik, Universität Augsburg, Universitätsstr. 1, Augsburg, Germany*
[3]*Deutsches Elektronen-Synchrotron, Notkestrasse 85, 22605, Hamburg, Germany*

(Received 7 June 2013; accepted 15 July 2013; published online 25 July 2013)

We have carried out time resolved stroboscopic diffraction experiments on standing surface acoustic waves (SAWs) of Rayleigh type on a $LiNbO_3$ substrate. A novel timing system has been developed and commissioned at the storage ring Petra III of Desy, allowing for phase locked stroboscopic diffraction experiments applicable to a broad range of timescales and experimental conditions. The combination of atomic structural resolution with temporal resolution on the picosecond time scale allows for the observation of the atomistic displacements for each time (or phase) point within the SAW period. A seamless transition between dynamical and kinematic scattering regimes as a function of the instantaneous surface amplitude induced by the standing SAW is observed. The interpretation and control of the experiment, in particular disentangling the diffraction effects (kinematic to dynamical diffraction regime) from possible non-linear surface effects is unambiguously enabled by the precise control of phase between the standing SAW and the synchrotron bunches. The example illustrates the great flexibility and universality of the presented timing system, opening up new opportunities for a broad range of time resolved experiments. [http://dx.doi.org/10.1063/1.4816801]

I. INTRODUCTION

Surface acoustic waves (SAWs) are an enabling technology for electromechanical frequency filters, micro-fluidic devices[1,2] as well as sensor applications.[3] Here we show that time resolved diffraction, combining structural resolution on the sub-$\AA$ scale with temporal resolution on the pico-second scale, allows for a direct observation of the atomistic displacements induced by standing SAWs in a $LiNbO_3$ crystal lattice. Towards this end a dedicated timing system has been designed and commissioned at beamline P08 of the low emittance storage ring Petra III at Desy, Hamburg, allowing for two distinct modes of time resolved synchrotron experiments as detailed in section II. With respect to earlier stroboscopic X-ray scattering experiments on SAWs,[4,5] the timing and read-out scheme used in this work, made possible by the favorable time structure of Petra III, more advanced detectors and the seamless integration into the beamline setup and control software, significantly enhances the experimental possibilities. Notably a precise control of phase ϕ between the acoustic wave and the synchrotron bunches allows for the observation of a seamless transition between dynamical and kinematic scattering regimes induced by the SAW (section IV). To the very best of our knowledge the presented measurements are the first stroboscopic time resolved experiments performed at Petra III.

[a]treusch@gwdg.de
[b]tsalditt@gwdg.de

The presented timing scheme is not limited to experiments using SAW excitation. It can be applied to a broader range of stroboscopic experiments, using e.g. laser, high voltage or microwave based excitation mechanisms.

II. TIME RESOLVED EXPERIMENTS AT P08 / PETRA III

The basic principle of a stroboscopic time resolved experiment is to match the frequency of a cyclic excitation (pump) with the repetition rate of short probe pulses. A precise variation of the time delay t between pump- and probe pulse allows to sample the dynamics induced by the pump pulse at a high number of time points. The temporal resolution is limited by probe pulse length and the overall jitter of the experimental setup. We start with a brief description the most important timing signals provided by the synchrotron storage ring. We then turn to a more detailed discussion on two distinct experimental configurations for time resolved x-ray experiments.

The revolution frequency of a synchrotron is approximately given by the circumference and the speed of light. More precisely, it depends on the energy E of the relativistic electron (or positron) in the storage ring, which in turn is set by the microwave frequency $f_{acc.}$ of the accelerating cavities. Furthermore, the filling mode of the storage ring determines the repetition rate f_b of the synchrotron bunches in an actual experiment. For Petra III the circumference of ≈2304 m leads to a revolution frequency of $f_{rev.} \approx 130.1$ kHz (microwave frequency $f_{acc.} \approx 499.564$ MHz, positron energy $E \approx 6$ GeV) and hence a bunch frequency of $f_b \approx 5.2$ MHz in the 40-bunch mode. Note that $f_{acc.}$ and hence f_b are known and stable during each experimental run but may vary by some Hz between succeeding runs (machine alignment / tuning). The temporal structure of Petra III is highly favorable for time resolved experiments since the individual bunches are equally spaced in the the storage ring. Hence no global phase factor or a distinction between individual X-ray pulses is necessary when synchronizing to the synchrotron frequency. Moreover, the temporal spacing of $\frac{1}{f_b} \approx 192$ ns between individual X-ray pulses is long enough for fast gating of modern pixel detectors, such as the Pilatus pixel detector (Dectris),[6] see e.g. Fig. 1(c).

In order to synchronize the SAW to the synchrotron bunch frequency f_b we used a modified version of the Petra III bunchclock. The bunchclock provides three independent and basically arbitrary integral dividers of the microwave frequency which can be used to synchronize pulsed excitation mechanisms (e.g. pulsed lasers) or to gate modern pixel detectors[6,7] to the bunch frequency f_b with phase stability. The exact frequency values and operating conditions of the storage ring are distributed to the bunchclocks via a modulated 40 MHz signal, see Fig. 1(a). Furthermore, a highly stable 10 MHz reference signal is distributed to every beamline which can be used in order to phase lock any external frequency- or delay generator to the synchrotron. This reference signal is generated from the microwave frequency by a rational divider. These timing capabilities lead to two modes of SAW excitation, see Fig. 2 for representative oscilloscope traces as taken during experiments in both modes:

In the first mode, standing SAWs (cw operation) at any integral multiple frequency $f_{SAW} = n \cdot f_b$ of the bunch frequency are generated by phase locking a frequency generator (SG384, Stanford Research Systems) to the 10 MHz reference, see Fig. 2(a). This allows for time resolved diffraction experiments without the need for a reduction of the effective X-ray frequency and hence flux by gated detectors[6] or high speed choppers.[8] The effective time delay t between SAW pump- and X-ray probe pulses can be set as a phase ϕ between the synchrotron pulses at f_b and the SAW signal at f_{SAW} directly on the frequency generator, time delay t and phase ϕ are related via $t = \frac{\phi}{360 \cdot f_{SAW}}$. ϕ is constantly monitored by a fast oscilloscope and implemented as a virtual counter in the measurement software (SPEC, Certified Scientific Software), temporal drift can hence be corrected for during data analysis. Due to uncertainties related to cable lengths and the electro-mechanical interaction at the IDTs, only relative values can be given for ϕ. An arbitrary 'phase zero' ϕ_0 (corresponding to e.g. nodes of the standing wave) is identified from the experimental results a posteriori (see section IV B).

In the second mode, short SAW pulses at a repetition rate of $f_{pp} = \frac{f_{acc.}}{499584} \approx 1$ kHz of the microwave frequency are applied by pulse modulation of the frequency generator, see Fig. 2(b). In order to warrant phase stability between the synchrotron frequency f_b and the pump-probe frequency

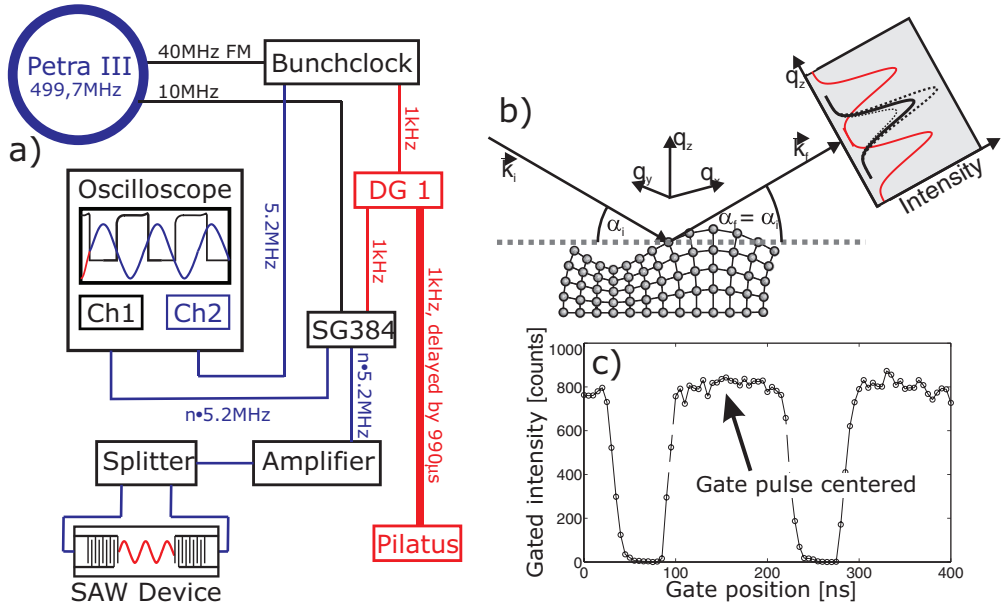

FIG. 1. a) Schematic of the timing system used for phase controlled time resolved X-ray diffraction. The Petra III bunchclock provides a signal corresponding to the respective bunch frequency (5.2 MHz in the 40-bunch mode) as well as a variety of preinstalled integral dividers. An accurate 10 MHz signal is used in order to lock a frequency generator (SG384) to the synchrotron frequency. The output from the frequency generator can be pulse modulated by a delay generator (DG1) in order to produce RF pulses, amplified and split in order to generate standing SAWs. b) Schematic of a phase locked time resolved diffraction experiment on a SAW distorted crystal lattice. The temporal evolution of shape and intensity of a single (i.e. the (*1,0,4*)) Bragg reflection is observed as a function of phase ϕ between the synchrotron pulses and a standing SAW. c) Individual X-ray pulses can be selected by gating the Pilatus detector with a second channel on DG1. The delay is adjusted so that the gate pulse overlaps with an individual X-ray bunch, as represented by the maxima of the gated intensity.

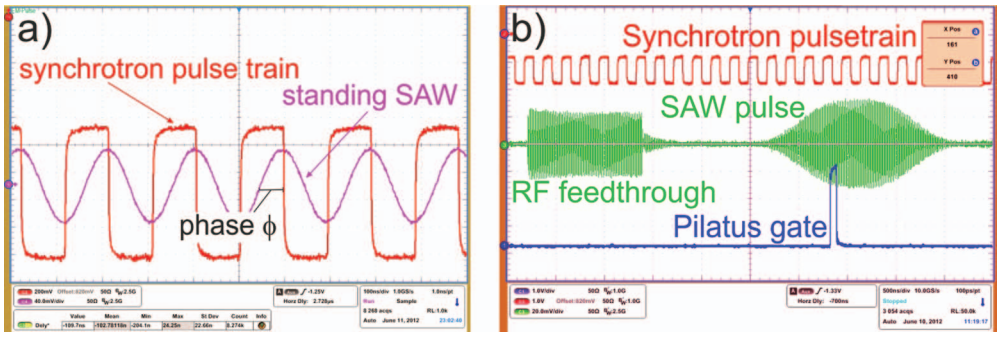

FIG. 2. a) Oscilloscope trace as taken during phase locked SAW generation. Successive synchrotron pulses (red) probe the standing SAW (blue) at a constant phase ϕ. b) Oscilloscope trace taken during a time resolved diffraction experiment using pulsed SAW excitation: The RF (SAW)-signal (green, $n \cdot 5.2$ MHz) is phase stable to both the X-ray pulse train (red, 5.2 MHz) as well as the gate pulses (blue, 1 kHz). The two RF pulses can be attributed to RF pickup (left pulse) and the propagating SAW pulse, broadened by the response function of the IDTs (right pulse).

f_{pp} a divider of $\frac{f_{acc.}}{f_{pp}} = 499584$ was chosen as an integral multiple of $\frac{f_{acc.}}{f_b} = 96$ for the 40-bunch mode, phase stability is thus also provided for the 60-, 240- and 960 bunch modes. In the case of pulsed (as opposed to cw) excitation mechanisms it is necessary to reduce the effective X-ray pulse frequency to match the pump frequency, so that only these X-ray pulses probing the structure at a well defined time delay with respect to the pump pulse are recorded. The advances of modern pixel detectors allow for an ultrafast gating of 2-D detectors without the need for high speed choppers. The time window of $\frac{1}{5.2\ \text{MHz}} = 192$ ns between two subsequent X-ray pulses is long enough to select and measure an individual X-ray pulse in the 5.2 MHz pulse train by gating a Pilatus 300 k 2-d detector

with nominally 50 ns short TTL pulses at a rate of ≈1 kHz, see Fig. 1(c). These gate ('probe') pulses have been produced by a Stanford Research Systems, DG535 delay generator (DG1 in Fig. 1(a)). The temporal delay between the gated synchrotron pulse and the modulated SAW pulse, as well as the width of the SAW pulse, can as well be controlled by DG1. Note that the effective length of the gate pulse provided by the Stanford Research Systems DG535 as observed by a fast oscilloscope is significantly shorter than 50 ns for a 50 Ω output load. Direct single pulse gating could also be demonstrated with a later version of the Petra III bunchclock, generating TTL output signals of a duration of 20 ns at $f_{pp} \approx 1$ kHz.

Both pump and gate pulses are referenced to a common trigger signal. In order to allow the pump pulse to be temporally ahead of the gate pulse, a pretrigger has to be generated. The gate pulse has hence been delayed by ≈990 μs on channel one of DG1 and fine tuned so that the gated intensity on the Pilatus detector is maximal, see Fig. 1(c). For a desired time delay of t the pump pulse is now delayed by 990 μs $- t$ on channel two of DG1 so that the excitation pulse arrives effectively ahead of the gate pulse.

III. MATERIALS AND METHODS

A. Surface acoustic wave generation

Piezoelectric materials offer the possibility to excite SAWs electrically:[9,10] A metallic comb-like finger structure is processed onto the surface by optical lithography and a RF voltage is applied to this so-called interdigital transducer (IDT), see Fig. 1(a). As the RF signal matches the design frequency $f^1_{SAW} = v_{SAW}/L^1_{SAW}$, which is given by the SAW velocity v_{SAW} and the finger periodicity L^1_{SAW} of the IDT, a SAW is excited and propagates along the sound path. In the present experiment this acoustically active region was 1 *mm* wide and was limited by a second IDT in a distance of 8 *mm*. This configuration of two opposing IDTs is called 'delay line', as a generated signal at one IDT is received by the other one with an acoustic delay due to the wave propagation. The basic parameters for SAW devices are given by (i) the piezoelectric substrate material and (ii) its crystallographic surface orientation (cut angle) in addition to the propagation direction on this surface. In this experiment, we use the very common so called '128° rot. Y cut' of $LiNbO_3$ as the X direction of this specific cut exhibits one of the highest coupling factors for electrical SAW excitation. However, here we used the direction perpendicular to X due to frequency constraints by the timing setup, as outlined above. The fundamental periodicity of the corresponding IDTs is designed to $L^1_{SAW} = 100$ μm and, with $v_{SAW} \approx 3670$ m/s, the fundamental frequency to $f^1_{SAW} = 36.7$ MHz. The finite frequency response of the device enables a SAW excitation at the synchrotron-locked frequency $f^1_{SAW} = 7 \cdot f_b = 36.4$ MHz. Due to the 'Split-3' layout of the IDTs, odd harmonics of the fundamental frequency can also be excited. In particular, we used the (locked) 5th harmonic $f^5_{SAW} = 182$ MHz, which corresponds to a wavelength of $L^5 = 20$ μm.

The SAW excited on 128° rot. Y $LiNbO_3$ in the direction perpendicular to X is a Rayleigh mode, so surface atoms follow an elliptical motion polarized in the sagittal plane (defined by SAW propagation direction and the surface normal, see Fig. 1(b)). The piezoelectricity of the substrate material induces an electric potential Φ which is linked to the deformation of the crystal. Both the deformation and Φ decay exponentially into the substrate, a detailed derivation of the solutions to the piezoelectric wave equations can e.g. be found in Ref. 10. The surface of 128° rot. Y cut $LiNbO_3$ is parallel to the *(1,0,4)* crystal plane (space group *R3c*), leading to a d-spacing of $d = 2.737$ Å for the first reflection along the q_z axis (unit cell constants $a = b = 5.1483$ Å, $c = 13.863$ Å, see e.g. Refs. 11 and 12).

It will be important to distinguish between the SAW amplitude H_1, denoting the instantaneous amplitude at the substrate surface and the amplitude $\sigma \propto H_1$, denoting the effective amplitude averaged over the penetration depth of the X-ray beam (corresponding to an effective mean square displacement).

We will refer to the nominal RF-power U after the RF amplifier (given in dBm, see Fig. 1(a)) when giving experimental numbers characterizing the intensity of the SAW, as the SAW intensity is assumed to be proportional to U. The SAW amplitude H_1 is proportional to $H_1 \propto \sqrt{U}$.

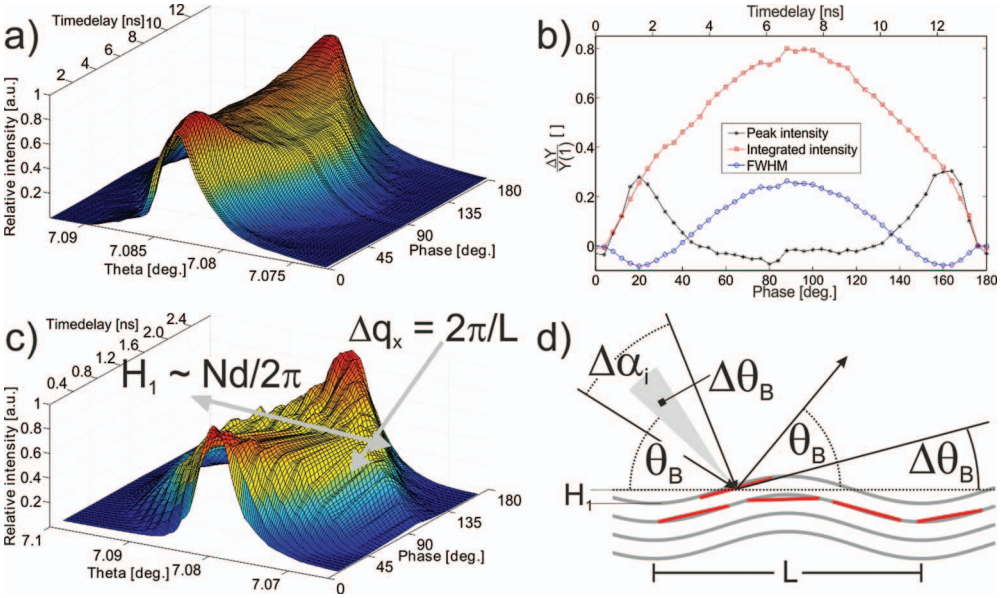

FIG. 3. a) Rocking curve of the $LiNbO_3$ *(1,0,4)* reflection as a function of phase (i.e. delay time) for SAW excitation by the 1st. harmonic frequency at $U = 27$ dBm. The broadening originates from side reflections (satellite peaks) induced by the SAW which can not be resolved experimentally. b) Relative changes $\frac{\Delta Y}{Y(1)}$ in peak intensity (stars, black), integrated intensity (squares, red), and full width at half maximum (FWHM, circles, blue) of the rocking curves shown in (a), as a function of phase ϕ. A sharpening of the reflection for $\phi \approx 20^\circ$ and $\phi \approx 160^\circ$ is observed accompanied by a steep increase of the intensity at the ridge of the rocking curve. This effect is attributed to an increased extinction length χ induced by the SAW, as detailed in the main text. A transition from dynamical to kinematic diffraction regimes occurs as soon as χ becomes equal to the linear attenuation length $1/\mu_x$. c) For smaller wavelengths, i.e. the 5th. SAW harmonic, distinct satellite reflections appear for $\phi \neq \phi_0$. The angular spacing $\Delta\theta = 0.0016^\circ$ of these side reflections is in perfect agreement with the expectation ($L^5_{SAW} = 20\ \mu$m for $f^5_{SAW} = 182$ MHz). From the number of observable diffraction satellites, the SAW amplitude can be determined.[17,21] d) The distortion of the crystal lattice due to a SAW leads to an increased acceptance angle $\Delta\theta_b$ of a given reflection. For an acceptance angle $\Delta\theta_b \leq \Delta\alpha_i$ (of the undistorted crystal lattice) smaller than the divergence $\Delta\alpha_i$ of the primary beam this will lead to an increased Bragg intensity. A rough estimation for $L = 100\ \mu$m and $H_1 = 3\ \mathring{A}$ yields an increase by $\approx$12 μrad.

B. X-ray diffraction setup

The diffraction experiments have been performed at an X-ray energy of 18 keV at the high resolution diffraction beamline P08, Petra III, DESY.[13] The sample was mounted vertically on a multi-circle diffractometer (Khozu NZD-3) in a horizontal scattering geometry, the X-ray beam being directed along the sound path of the SAW device. To ensure a perfect overlap of the X-ray beam with the acoustically excited area of the SAW device, the beam was collimated to 55 $\mu m \times 290\ \mu$m (h,v) using a slit system at a distance of $\approx$1 m as well as a set of collimating CRLs at a distance of 30 m in front of the sample. The X-ray attenuation length of 28 μm in $LiNbO_3$ for the *(1,0,4)* Bragg reflection ($\theta = 7.2306^\circ$ at $E = 18\ keV$) is well below the penetration length of the SAW, which is on the order of the acoustic wavelength. The horizontal beam size of 55 μm leads to a footprint of 411 μm along the sample surface for the *1,0,4* reflection, hence only the acoustically excited substrate volume is probed by the X-ray beam. The energy bandwidth after the *Si*111 high heat-load monochromator and the *Si*311 large offset monochromator was $\frac{\Delta E}{E} \approx 6 \cdot 10^{-5}$. Time resolved reflectivity and rocking measurements on standing SAWs were performed using a NaI scintillation counter (Cyberstar, Oxford), the angular step size of $\left(\frac{1}{10000}\right)^\circ$ for the rocking measurements (Fig. 3) was limited by the mechanical resolution of the Khozu Diffractometer. The nominal horizontal beam divergence in the P08 collimation mode is $\Delta\alpha_i \approx 8\ \mu rad = \left(\frac{5}{10000}\right)^\circ$ (FWHM). The actual horizontal beam divergence as the minimal angular spacing between distinguishable diffraction satellites was measured to be $\Delta\alpha_i \approx 28\ \mu$rad (FWHM) during the experiment, see section IV B.

IV. ULTRAFAST TRANSITION BETWEEN DYNAMICAL AND KINEMATIC DIFFRACTION REGIMES IN *LiNbO*$_3$ EXCITED BY SAWS

Two kinds of time resolved X-ray measurements have been performed in order to study ultrafast SAW induced atomistic displacements in the $LiNbO_3$ crystal lattice.

(i) Rocking measurements around the $LiNbO_3$ *(1,0,4)* Bragg reflection have been recorded for different phases ϕ between the standing wave and the synchrotron bunches, corresponding to different time delays $t = \frac{\phi}{360 \cdot f_{SAW}}$. The SAW intensity was $U = 27$ dBm, experiments have been performed at the first f^1_{SAW} and fifth f^5_{SAW} harmonic SAW frequency.

(ii) Time resolved intensity traces $I(U, \phi)$ of the $LiNbO_3$ *(1,0,4)* Bragg reflection have been recorded as a function of ϕ for a given SAW RF-amplitude U at a fixed angle of incidence (Bragg angle).

Standing SAWs (cw excitation) have been applied in all cases, diffraction signals have been recorded stroboscopicly without the need for high speed gating or individual pulse selection, see section II. A typical oscilloscope trace as taken during phase locked stroboscopic experiments is depicted in Fig. 2(a). While time resolved rocking measurements are a valuable tool to disentangle the complex interplay between dynamical, kinematic and possible sample related effects, time resolved intensity traces $I(U, \phi)$ over a broader range of SAW intensities U help to prove the correctness of these interpretations and to further illustrate the experimental capabilities enabled by the timing scheme introduced in this paper.

While we will refer to the phase ϕ between the standing SAW at $f_{SAW} = n \cdot f_b$ and the synchrotron bunches at f_b as the generic temporal coordinate for cw waves throughout the discussion, let us just shortly emphasize the close relation of ϕ to the temporal delay $t = \frac{\phi}{360} \cdot \frac{1}{f_{SAW}}$. The step width of $\Delta\phi = 1^\circ$ (limited by the RF frequency generator, see Fig. 1(a)) limits the temporal resolution to $\Delta t = \frac{1}{360} \cdot \frac{1}{f_{SAW}} \approx 76$ ps in case of the first harmonic SAW frequency $f^1_{SAW} = 36.4$ MHz.

A. General remarks on expected dynamical and kinematic diffraction effects

The interpretation of the observed intensity variations is based on scattering related effects, in particular on a SAW induced transition from dynamical to kinematic scattering regimes. Alternative explanations based e.g. on non-linear acoustic effects (i.e. higher acoustic harmonic generation) or temperature induced modifications of the SAW resonator have been carefully studied, but can not explain our experimental findings in full detail. To therefore facilitate the understanding of the complex interplay between diffraction related and sample related effects, three main remarks on x-ray diffraction from a SAW distorted crystal lattice will be given, before we turn to the discussion of the experimental data in sections IV B and IV C. In particular the need for dynamical diffraction theory will be motivated, providing a phenomenological description of extinction related effects. For $LiNbO_3$ both extinction length and absorption length are of the same order of magnitude, as detailed below, so that the dynamical scattering of the perfect crystal can be modified by small changes in real structure (mosaicity) resulting in an increase of diffraction intensity. We will, however, treat this issue in rather simple terms. A detailed description of dynamical and kinematic scattering in terms of a unified and complete theory, for example as presented in Ref. 14 is beyond the scope of this paper which focuses on a proof of principle of phase stabilized time-resolved diffraction.

The instantaneous Debye Waller factor:

For standing waves $I(U, \phi)$ can in a first basic approach be understood in terms of the instantaneous Debye Waller factor $I(U, \phi) \propto e^{-q_z^2 \sigma(U,\phi)^2}$, with the effective mean square displacement $\sigma(U, \phi)$ being proportional to the amplitude H_1 of the standing wave (in good approximation also proportional to the amplitude $\propto \sqrt{U}$ of the SAW exciting RF signal) and varying harmonically with the phase ϕ. At an instant ϕ_0 the x-ray pulses probe the node of the standing wave, the apparent $\sigma(U, \phi)$ is hence that of an undistorted substrate and the integrated Bragg-intensity is at its maximum level. At a phase of $\phi_0 + 90^\circ$ the x-ray pulses probe the crest of the standing wave, leading to a minimum of the diffracted intensity.

Kinematic approximation – Satellite reflections corresponding to a harmonically distorted crystal lattice:
Depending on the acoustic wavelength of the SAW, diffraction satellites arising from the SAW modulated substrate[15] contribute to the resulting phase and amplitude dependent intensity traces $I(U, \phi)$. In case of the fifth harmonic SAW frequency ($f^5_{SAW} = 182$ MHz, $L^5_{SAW} = 20\ \mu$m) the angular spacing of $\Delta\theta \approx 0.0016^\circ = 28\ \mu$rad between adjacent diffraction satellites can just be resolved in the time resolved rocking measurements (see section IV B) and has thus been used as an estimate for the beam divergence $\Delta\alpha_i \approx 28\ \mu$rad in the horizontal scattering plane. In case of the first harmonic SAW frequency ($f^1_{SAW} = 36.4$ MHz, $L^1_{SAW} = 100\ \mu$m) a beam divergence of $\Delta\alpha_i \approx 28\ \mu$rad leads to an integration over approximately $N = 5$ diffraction satellites.
Dynamical diffraction:
Dynamical diffraction effects have to be taken into account for diffraction experiments on highly oriented $LiNbO_3$ single crystals.[16,17] Extinction effects strongly influence the shape and intensity of individual Bragg reflections since the linear attenuation length $1/\mu_x \approx 27.3\ \mu$m[18] is more than one order of magnitude larger than the extinction length $\chi \approx 1.2\ \mu$m for the undistorted $LiNbO_3$ *(1,0,4)* reflection. Furthermore the Darwin width $\Delta\theta_D = 18.6\ \mu$rad[19] of the *(1,0,4)* Bragg reflection is significantly smaller than the horizontal beam divergence of $\Delta\alpha_i \approx 28\ \mu$rad, an angular integration is therefore performed even without sample rotation. It is then straightforward to show that a small distortion, or an increase in mosaicity and hence acceptance angle $\Delta\theta_B$, leads to an increase of the integrated intensity (see Fig. 3) rather than a decrease with respect to a perfectly ordered crystal lattice. In other words, the increase in extinction length in the dynamical theory of x-ray diffraction[20] over-compensates the intensity decrease due to the Debye Waller factor in the kinematic approximation.

B. Time (i.e. phase ϕ) resolved rocking measurements

The two characteristic length scales of the SAW, namely its wavelength L and its amplitude H_1, can be extracted from time (i.e. phase ϕ) resolved rocking curves around the *(1,0,4)* Bragg reflection, see Fig. 3. As shown in Ref. 21, the transverse acoustic amplitude $H_1 = \frac{Nd}{2\pi}$ can be expressed in terms of the inter planar spacing $d = 2.5741$ Å of the *1,0,4*- reflection and the number of observable satellite reflections N. For the first harmonic SAW frequency $f^1_{SAW} = 36.4$ MHz as depicted in Fig. 3(a), the instrumental resolution is however not sufficient to distinguish between individual satellite reflections since $q_x = \frac{2\pi}{\lambda}(\cos(\alpha_i) - \cos(\alpha_f)) = \frac{2\pi}{L}$ becomes too small for large L. In case of the fifth harmonic frequency $f^5_{SAW} = 182$ MHz (see Fig. 3(c)) individual diffraction satellites can just be resolved, the amplitude is determined to $H_1 = 3.51$ Å for $U = 27$ dBm. The angular spacing of $\Delta\theta = 0.0016^\circ$ between subsequent diffraction satellites is in perfect agreement with the expectation for the SAW wavelength ($L^5_{SAW} = 20\ \mu$m for $f^5_{SAW} = 182$ MHz).

Let us briefly discuss the rocking curve measurements in terms of dynamical and kinematic diffraction effects. Without SAW or at nodes of the standing waves the $LiNbO_3$ single crystal is perfect enough to be described by dynamical diffraction.[16,17] When the amplitude of the SAW increases, the extinction length χ is extended by the strain field of the SAW, equivalent to an increased mosaicity and hence acceptance angle $\Delta\theta_B$, see Fig. 3(d). The prolonged extinction length leads to an increase of the peak intensity as well as a decrease of the rocking width in the dynamical diffraction regime. A transition from mostly dynamical scattering to regimes dominated by kinematic diffraction occurs as soon as χ becomes comparable to the linear attenuation length $1/\mu_x$. This transition is marked by the minimum of the rocking scan width as well as the maximum of the peak intensity at $\phi \approx 20^\circ$ and $\phi \approx 160^\circ$ in Fig. 3(b). Since the SAW amplitude oscillates as a standing wave, this transition occurs at $4 f_{SAW}$ (for increasing / decreasing amplitudes as well as positive and negative displacements).

Let us now identify the nodes of the standing wave, denoted as ϕ_0, on the basis of the data depicted in Fig. 3(b). Nodes of the standing SAW strictly occur at a phase difference of $\Delta\phi = 180^\circ$, therefore the minima of the FWHM curve, separated by $\Delta\phi \approx 140^\circ$, can not correspond to nodes of the standing wave, in line with the interpretation as a soft transition from dynamical to kinematic diffraction regimes. Instead, $\phi_0 \approx 0^\circ$ can be identified with the minimum of the integrated intensity

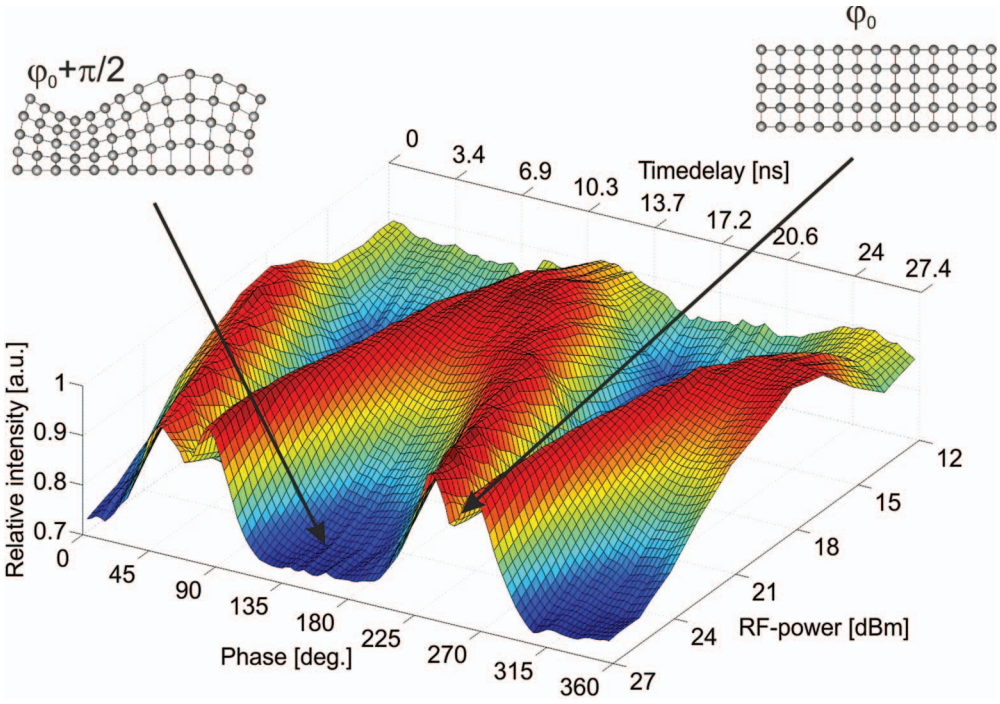

FIG. 4. The intensity of the $LiNbO_3$ *1,0,4*-Bragg reflection measured as a function of phase ϕ, and SAW intensity U, as recorded for the 1st. harmonic SAW frequency. A harmonic intensity trace directly reproducing the SAW frequency is observed for $U \leq 17$ dBm. For $U \geq 17$ dBm, a splitting of the intensity maxima is observed. In the main text, this pattern is interpreted based on a transition from dynamical to kinematic diffraction regimes.

in Fig. 3(b). This interpretation is justified by the observation that, in contrast to the peak intensity, the integrated intensity follows the SAW excitation with a sinusoidal response, which is expected since it corresponds to the sum over $N \geq 5$ experimentally unresolved side reflections (satellites). The intensity of these satellites increases with the instantaneous SAW amplitude H_1[15] and can be described in kinematic approximation. The further interpretation of the intensity traces $I(U, \phi)$ below is based on this identification of ϕ_0 and the assumption that a *mild* increase of SAW amplitude leads to an increase of the peak intensity due to a reduction of extinction effects (dynamical diffraction theory) whereas high SAW amplitudes lead to a decrease of diffraction intensity due to the Debye-Waller factor in kinematic diffraction theory. This view is further supported by the U dependence of $I(U, \phi)$ as discussed in section IV C.

C. Intensity traces $I(U, \phi)$

Let us now turn to the $I(U, \phi)$ dataset for the 1st harmonic frequency ($f^1_{SAW} = 36.4$ MHz $= 7 \cdot f_b$) depicted in Fig. 4. For $U \leq 17$ dBm, $I(U, \phi)$ is well described by the $\Delta I \propto \sin^2(f_{SAW})$ behavior, which is expected for purely dynamical diffraction effects. It essentially corresponds to a single standing wave of frequency f^1_{SAW}. For $U \geq 17$ dBm, a splitting of the maxima in $I(U = const., \phi)$ is observed, indicating a transition from dynamical to kinematic diffraction regimes. We therefore put forward the interpretation based on an interplay between kinematic and dynamical diffraction effects, in line with the argumentation presented in section IV B. For SAW intensities $U \leq 17$ dBm crests of the standing wave lead to an increase in diffraction intensity due to dynamical effects, as discussed in the context of the time resolved rocking curves. For $U \geq 17$ dBm, linear absorption of X-ray radiation dominates over extinction effects, a transition from dynamical to kinematic diffraction regimes takes place. Now the peak amplitude of the standing wave leads to a decrease of diffraction intensity due to the Debye-Waller factor.

V. CONCLUSION

It was shown that the strain field induced by standing SAWs leads to a seamless transition from dynamical to kinematic diffraction regimes for a highly ordered $LiNbO_3$ crystal lattice on the 100 ps timescale. An exact description of the observed effects in terms of detailed dynamical and kinematic diffraction equations (and especially a unified theory as e.g. derived in Ref. 14) is beyond the scope of this paper, but it becomes evident that the accurate control of phase between the standing acoustic wave and the synchrotron bunches has proven to be absolutely indispensable for the data interpretation. It has to be concluded that, independent of the underlying most likely scattering related mechanism, time resolved X-ray diffraction experiments serve as an unique tool to directly probe the atomistic displacements induced by SAWs. Measurement artifacts evoked by any electronic or mechanical effects in the IDTs can be excluded. The timing scheme of Petra III has been proven to be highly accurate and stable, its great flexibility will be highly beneficial for a broad range of time resolved X-ray experiments at Petra III.

ACKNOWLEDGMENTS

We thank Dr. Oliver Seeck and Kathrin Pflaum for excellent support prior to as well as during the synchrotron experiment at P08, Petra III. Furthermore we thank Hans-Thomas Duhme and Jens Klute (MSK group, DESY) for their fast and uncomplicated modification of the Petra III bunchclock, as well as Dr. Karl Lautscham for important support in electronics. Support by the German Research Foundation (Deutsche Forschungsgemeinschaft, DFG) through SFB 937 as well as the Courant Research Centre "Nano-Spectroscopy and X-Ray Imaging" is gratefully acknowledged. Part of this work has been sponsored by the German Initiative of Excellence under the 'Nanosystems Initiative Munich (NIM)".

[1] Z. Guttenberg, A. Rathgeber, S. Keller, J. O. Raedler, A. Wixforth, M. Kostur, M. Schindler, and P. Talkner, "Flow profiling of a surface-acoustic-wave nanopump," Phys. Rev. E **70**(5), 056311 (2004).
[2] T. Franke, "Surface acoustic wave (saw) directed droplet flow in microfluidics for pdms devices," Lab on a chip **9**(18), 2625 (2009).
[3] Kerstin Laenge, Bastian Rapp, and Michael Rapp, "Surface acoustic wave biosensors: a review," Analytical and Bioanalytical Chemistry **391**(5), 1509–1519 (2008).
[4] W. Sauer, M. Streibl, T. H. Metzger, A. G. C. Haubrich, S. Manus, A. Wixforth, J. Peisl, A. Mazuelas, J. Hartwig, and J. Baruchel, "X-ray imaging and diffraction from surface phonons on gaas," Applied Physics Letters **75**(12), 1709–1711 (1999).
[5] E. Zolotoyabko, "Time and phase control of x-rays in stroboscopic diffraction experiments," Review of scientific instruments **73**(3), 1643 (2002).
[6] T. Ejdrup, H. T. Lemke, K. Haldrup, T. N. Nielsen, D. A. Arms, D. A. Walko, A. Miceli, E. C. Landahl, E. M. Dufresne, and M. M. Nielsen, "Picosecond time-resolved laser pump/x-ray probe experiments using a gated single-photon-counting area detector," Journal of Synchrotron Radiation **16**(3), 387–390 (2009).
[7] A. Miceli, "Application of pixel array detectors at x-ray synchrotrons," Journal of Instrumentation **4**(03), P03024 (2009).
[8] Michael Wulff, Anton Plech, Laurent Eybert, Rudolf Randler, Friedrich Schotte, and Philip Anfinrud, "The realization of sub-nanosecond pump and probe experiments at the esrf," Faraday Discuss. **122**, 13–26 (2003).
[9] Lord Rayleigh, "On waves propagated along the plane surface of an elastic solid," Proceedings of the London Mathematical Society **s1-17**(1), 4–11 (1885).
[10] Herbert Matthews, *Surface wave filters design, construction, and use* (Wiley, 1977).
[11] S. C. Abrahams, J. M. Reddy, and J. L. Bernstein, "Ferroelectric lithium niobate. 3. single crystal x-ray diffraction study at 24c," Journal of Physics and Chemistry of Solids **27**, 997–1012 (1966).
[12] R. S. Weis and T. K. Gaylord, "Lithium niobate: Summary of physical properties and crystal structure," Applied Physics A: Materials Science & Processing **37**, 191–203 (1985).
[13] O. H. Seeck, C. Deiter, K. Pflaum, F. Bertam, A. Beerlink, H. Franz, J. Horbach, H. Schulte-Schrepping, B. M. Murphy, M. Greve, and O. Magnussen, "The high-resolution diffraction beamline p08 at petra iii," Journal of Synchrotron Radiation **19**(1), 30–38 (2012).
[14] P. B. Hirsch and G. N. Ramachandran, "Intensity of x-ray reflexion from perfect and mosaic absorbing crystals," Acta Crystallographica **3**(3), 187–194 (1950).
[15] R. Tucoulou and Dimitry Roshchupkin F. de Bergevin, O. Mathon, "X-ray bragg diffraction of *linbo*$_3$ crystals excited by surface acoustic waves," Phys. Rev. B **64**(13), 134108 (2001).
[16] W. Sauer, T. H. Metzger, J. Peisl, Y. Avrahami, and E. Zolotoyabko, "X-ray diffraction under surface acoustic wave excitation," Physica B: Condensed Matter **248**(1-4), 358–365 (1998).

[17] Igor A. Schelokov, Dmitry V. Roshchupkin, Dmitry V. Irzhak, and Remi Tucoulou, "Dynamical theory for calculations of x-ray spectra from crystals modulated by surface acoustic waves," Journal of Applied Crystallography **37**(1), 52–61 (2004).
[18] http://henke.lbl.gov/optical_constants/atten2.html.
[19] http://sergey.gmca.aps.anl.gov/x0h.html.
[20] J. Als-Nielsen, *Elements of Modern X-Ray Physics* (Wiley, 2001).
[21] R. Tucoulou, R. Pascal, M. Brunel, O. Mathon, D. V. Roshchupkin, I. A. Schelokov, E. Cattan, and D. Remiens, "X-ray diffraction from perfect silicon crystals distorted by surface acoustic waves," Journal of Applied Crystallography **33**(4), 1019–1022 (2000).